

# Disentangling the Effects of Structure and Lone-Pair Electrons in the Lattice Dynamics of Halide Perovskites

Sebastián Caicedo-Dávila,<sup>1</sup> Adi Cohen,<sup>2</sup> Silvia G. Motti,<sup>3,4</sup> Masahiko Isobe,<sup>5</sup> Kyle M. McCall,<sup>6,7,\*</sup> Maksym V. Kovalenko,<sup>6,7</sup> Omer Yaffe,<sup>2</sup> Laura M. Herz,<sup>3,8</sup> Douglas H. Fabini,<sup>5,9,†</sup> and David A. Egger<sup>1,‡</sup>

<sup>1</sup>*Physics Department, TUM School of Natural Sciences, Technical University of Munich, 85748 Garching, Germany*

<sup>2</sup>*Department of Chemical and Biological Physics, Weizmann Institute of Science, Rehovot 76100, Israel*

<sup>3</sup>*Clarendon Laboratory, Department of Physics, University of Oxford, Parks Road, Oxford, OX1 3PU, United Kingdom*

<sup>4</sup>*School of Physics and Astronomy, Faculty of Engineering and Physical Sciences, University of Southampton, University Road, Southampton SO17 1BJ, United Kingdom*

<sup>5</sup>*Max Planck Institute for Solid State Research, 70569 Stuttgart, Germany*

<sup>6</sup>*Laboratory of Inorganic Chemistry, Department of Chemistry and Applied Biosciences, ETH Zurich, CH-8093 Zürich, Switzerland.*

<sup>7</sup>*Laboratory for Thin Films and Photovoltaics, EMPA - Swiss National Laboratories for Materials and Technology, CH-8600 Dübendorf, Switzerland*

<sup>8</sup>*TUM Institute for Advanced Study, Technische Universität München, 85748 Garching, Germany*

<sup>9</sup>*Department of Chemistry, Massachusetts Institute of Technology, 02139 Cambridge, MA, USA*

Metal halide perovskites have shown great performance as solar energy materials, but their outstanding optoelectronic properties are paired with unusually strong anharmonic effects. It has been proposed that this intriguing combination of properties derives from the “lone pair” electrons of the octahedral metal cations, but the precise impact of this chemical feature remains unclear. Here we show that in fact a lone pair of electrons is not a prerequisite for the strong anharmonicity and low-energy lattice dynamics encountered in this class of materials. We combine X-ray diffraction, infrared and Raman spectroscopies, and first-principles molecular dynamics calculations to directly contrast the lattice dynamics of CsSrBr<sub>3</sub> with those of CsPbBr<sub>3</sub>, two compounds which bear close structural similarity but with the former lacking lone pairs on the octahedral metal. We exploit low-frequency diffusive Raman scattering, nominally symmetry-forbidden in the cubic phase, as a fingerprint to detect anharmonicity and reveal that low-frequency tilting occurs irrespective of lone pair presence. This work highlights the key role of structure in perovskite lattice dynamics, providing important design rules for the emerging class of soft perovskite semiconductors for optoelectronic and light-harvesting devices.

Halide perovskites (HaPs) with formula AMX<sub>3</sub> generated enormous research interest because of their outstanding performance in optoelectronic devices, most notably in efficient solar cells.<sup>1–3</sup> These compounds are highly unusual among the established semiconductors because they feature an intriguing combination of properties. Strong anharmonic fluctuations<sup>4–6</sup> in these soft materials appear together with optoelectronic characteristics that are favorable for technological applications.<sup>7,8</sup> This confluence raised puzzling questions regarding the microscopic characteristics of the materials and the compositional tuning of their properties alike. On the one hand, the soft anharmonic nature of the HaP structure may be beneficial in self-healing mechanisms of the material,<sup>9–11</sup> allowing for low-energy synthesis routes in their fabrication. On the other hand, pairing of anharmonic fluctuations and optoelectronic processes for key quantities of HaPs, *e.g.*, band gaps,<sup>12–15</sup> optical absorption profiles,<sup>16–18</sup> and charge-carrier mobilities,<sup>8,19–25</sup> exposed incomplete microscopic rationales for the fundamental physical processes involved in solar-energy conversion. Established materials design rules are now being challenged by these observations, opening a gap in our protocols for making improved compounds.

Significant efforts are now underway to discern the chemical effects giving rise to these remarkable properties of HaPs. Because lattice dynamical and optoelectronic properties appear both to be special and coupled in unusual ways, a common origin in chemical bonding could underlie these phenomena. In this context, an interesting chemical feature is that the octahedral cations in these compounds often bear an ns<sup>2</sup> electron configuration (*e.g.*, Pb<sup>2+</sup> with configuration [Xe]6s<sup>2</sup>), which is not present in many other semiconductors.<sup>26</sup> This particular aspect of HaPs can lead to formation of a lone pair of electrons (LPE) that impacts crystal structures and lattice dynamics<sup>27–30</sup> as well as ionic dielectric responses.<sup>26,28,31,32</sup> At the same time, the LPE plays a role in optoelectronic properties of these materials: its influence on the dielectric function can modify the Coulomb screening that is relevant for small exciton binding energies, reduced recombination rates and other key properties of HaPs.<sup>33,34</sup>

Confluences of the LPE with structural and lattice-dynamical properties were investigated in previous work exploring the chemical space of HaPs. Gao *et al.*<sup>30</sup> found an inverse relationship between the Goldschmidt tolerance factor, *t*,<sup>35</sup> and anharmonic octahedral tilting motions. Similarly, Huang *et al.* varied the A-site cation

to explore interrelations of chemical, structural, and dynamical effects in HaPs,<sup>32</sup> reporting  $t$ -induced modulations of octahedral tiltings and LPE stereoactivity. A recent study by several of the present authors found that  $\text{Cs}_2\text{AgBiBr}_6$  lacks some expressions of lattice anharmonicity found in other HaP variants.<sup>36</sup> Because every other octahedral cation ( $\text{Ag}^+$ ) cannot form a LPE in this compound, changing the electron configuration of the cations may also suppress certain aspects of the lattice dynamics in HaPs. Taken together, previous work assigned a central role of the LPE in the anharmonic lattice dynamics of HaPs in addition to its established effect on the electronic structure and dielectric screening. However, exploring the chemical space of HaPs in this way simultaneously changes their structures. Therefore, isolating the convoluted occurrences of LPE- and purely structurally-determined changes in the lattice dynamics of HaPs remained challenging, making an assessment of the precise impact of LPE on anharmonicity in these soft semiconductors largely inaccessible.

Here, we address this issue and show that presence of a LPE is not required for the strong anharmonicity in the low-energy lattice dynamics of soft HaP semiconductors. We disentangle structural and chemical effects in the lattice dynamics of HaPs by comparing the well-known  $\text{CsPbBr}_3$  with the far less studied  $\text{CsSrBr}_3$ . Both exhibit almost identical geometrical and structural parameters, but  $\text{CsSrBr}_3$  cannot form a LPE at the M-site owing to the noble gas electron configuration of  $\text{Sr}^{2+}$ , allowing separation of the effects of the LPE and the geometry on the lattice dynamics in a direct manner. Combining electronic structure and molecular dynamics (MD) calculations with X-ray diffraction (XRD), infrared (IR) and Raman spectroscopies, we assess a key fingerprint of vibrational anharmonicity, *i.e.*, the Raman central peak, which is a broad peak towards zero frequency in the Raman spectrum resulting from diffusive inelastic scattering.<sup>26,30–32,37–39</sup> While the electronic structure and dielectric properties of  $\text{CsPbBr}_3$  and  $\text{CsSrBr}_3$  are very different, their vibrational anharmonicities are found to be remarkably similar. In particular, the crucial dynamic octahedral tiltings giving rise to the Raman central peak are still present even in absence of the LPE in  $\text{CsSrBr}_3$ . Our results provide microscopic understanding of precisely how the LPE influences the anharmonic octahedral tiltings that dynamically break the average cubic symmetry in both compounds, and rule out the LPE stereoactivity as the sole reason for appearances of such anharmonicity in soft HaPs. These findings are important for chemical tuning of HaPs needed for new materials design.

## RESULTS

### Electronic structure and bonding

We first investigate the electronic structure and bonding of  $\text{CsPbBr}_3$  and  $\text{CsSrBr}_3$  using density-functional theory (DFT). Figure 1 shows their band structure, total and

projected density of states (DOS), as well as the total and projected crystal-orbital Hamilton population (COHP) of the high-temperature cubic phases of  $\text{CsPbBr}_3$  and  $\text{CsSrBr}_3$ . The electronic band structure and bonding of  $\text{CsPbBr}_3$  were extensively investigated before:<sup>40</sup> the conduction band minimum (CBM) is formed by anti-bonding interactions (positive COHP in Figure 1c) between Pb-6p and Br-4p/Br-4s orbitals, while the valence band maximum (VBM) is formed by anti-bonding interactions between Br-4p and Pb-6s orbitals, where the nominally filled 6s orbital of  $\text{Pb}^{2+}$  allows the possible formation of a LPE.

The electronic structure of  $\text{CsSrBr}_3$  exhibits entirely different characteristics,<sup>26,41</sup> especially a much larger band gap and weaker covalent interactions. Notably, the magnitude of the COHP is significantly reduced with respect to that of  $\text{CsPbBr}_3$ , indicating much greater ionicity, and the COHP is almost entirely recovered by interactions between Cs and Br. Importantly, all bands derived from antibonding interactions between Sr-5s and Br-4p/Br-4s

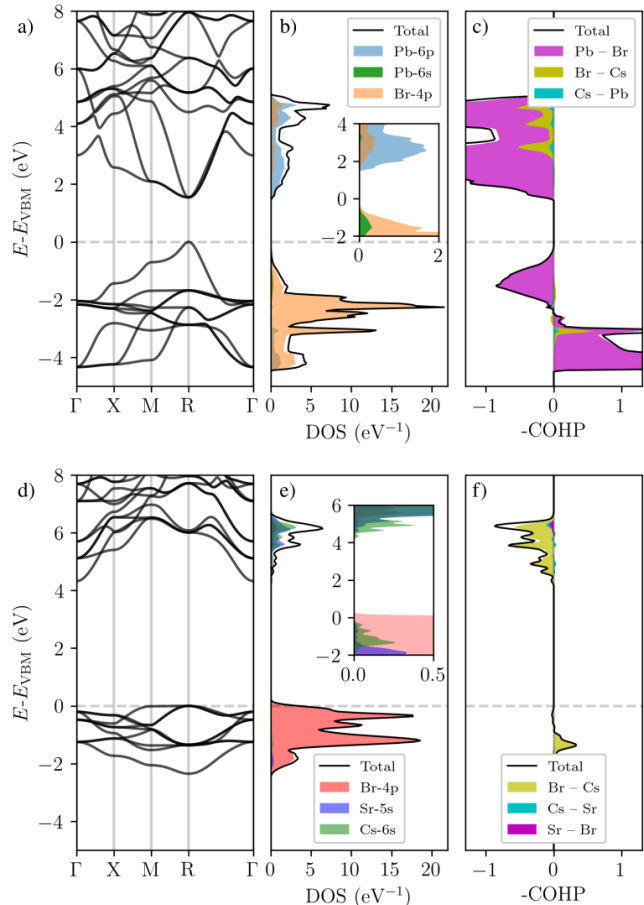


FIG. 1. **Electronic structure.** DFT-computed electronic band structure of cubic  $\text{CsPbBr}_3$  (panel a) and corresponding total and projected density of states (DOS, panel b) and crystal-orbital Hamilton population (COHP, panel c). Panels d–f show the same data for  $\text{CsSrBr}_3$ .

TABLE I. **Dielectric properties of cubic CsMBr<sub>3</sub>.** Dielectric constant in the high-frequency limit with respect to the optical phonon mode frequencies,  $\epsilon_\infty$ , and Born effective charges,  $Z_i^*$ , of cubic CsPbBr<sub>3</sub> and CsSrBr<sub>3</sub> as calculated by DFT. We report  $Z_{\text{Br}}^*$  for the Br bonded with Pb/Sr along the  $z$  axis.

Compound	$\epsilon_\infty$	$Z_{\text{Cs}}^*$	$Z_{\text{M-site}}^*$	$Z_{\text{Br}}^*$ ( $xx, yy, zz$ )
CsPbBr <sub>3</sub>	5.39	1.38	4.33	(-0.63, -0.63, -4.46)
CsSrBr <sub>3</sub>	3.02	1.35	2.43	(-0.91, -0.91, -1.97)

are empty due to the electron configuration of Sr<sup>2+</sup> ([Kr]), and there is no potential for lone pair formation on Sr<sup>2+</sup>. A manifestation of the lack of a lone-pair-compatible electron configuration in CsSrBr<sub>3</sub> is that there is no cross-gap hybridization of the halide valence orbitals. By contrast, Br-4*p* orbitals hybridize with Pb-6*p* across the gap of CsPbBr<sub>3</sub> (see the pCOHP in Figure 1c). This leads to large Born effective charges, *i.e.*, large changes in the macroscopic polarization upon ionic displacements<sup>42-45</sup> reported in Table I, which for CsPbBr<sub>3</sub> are more than double the formal charge of Pb (+2) and Br (-1) and much larger than the corresponding values for CsSrBr<sub>3</sub>. Similarly, there is also a larger electronic contribution to the dielectric response in CsPbBr<sub>3</sub> and it features a larger value of the dielectric function at the high-frequency limit ( $\epsilon_\infty$ ) compared to CsSrBr<sub>3</sub>.

### Structural properties and phase transitions

In spite of the markedly different electronic structure and bonding characteristics, CsSrBr<sub>3</sub> and CsPbBr<sub>3</sub> exhibit the same high-temperature cubic crystal structure ( $Pm\bar{3}m$ ) and very similar lattice parameters (see Supplementary Information). One can rationalize this through the nearly identical ionic radii of Pb<sup>2+</sup> and Sr<sup>2+</sup> (119 and 118 pm) and the resulting Goldschmidt factors for the compounds (0.862 and 0.865). Furthermore, both materials exhibit the same sequence of structural phase transitions from the high-temperature cubic to the low-temperature orthorhombic phase (with an intermediate tetragonal phase), as shown by temperature-dependent lattice parameters in Figure 2 that were determined *via* XRD. The cubic-to-tetragonal phase transition temperature of CsSrBr<sub>3</sub> ( $\sim 520$  K) is noticeably higher than that of CsPbBr<sub>3</sub> ( $\sim 400$  K)<sup>46,47</sup> and slightly higher ( $\sim 10$  K) than that reported for Eu-doped CsSrBr<sub>3</sub>:Eu 5%.<sup>48</sup> The volumetric thermal expansion coefficient ( $\alpha_V$ ) of CsSrBr<sub>3</sub> ( $\sim 1.32 \times 10^{-4} \text{ K}^{-1}$  at 300 K) is large and similar to that of CsPbBr<sub>3</sub> ( $\sim 1.29 \times 10^{-4} \text{ K}^{-1}$ , see the Supplementary Information for details), in good agreement with the one reported for CsSrBr<sub>3</sub>:Eu.<sup>48</sup> Just as for other inorganic HaPs,  $\alpha_V$  of CsSrBr<sub>3</sub> slightly decreases with temperature.<sup>49,50</sup> The similarity of geometric factors and structural phase transitions suggests that the octahedral tilting dynamics in CsSrBr<sub>3</sub> might be similar to those in CsPbBr<sub>3</sub>, which contrasts with their markedly different

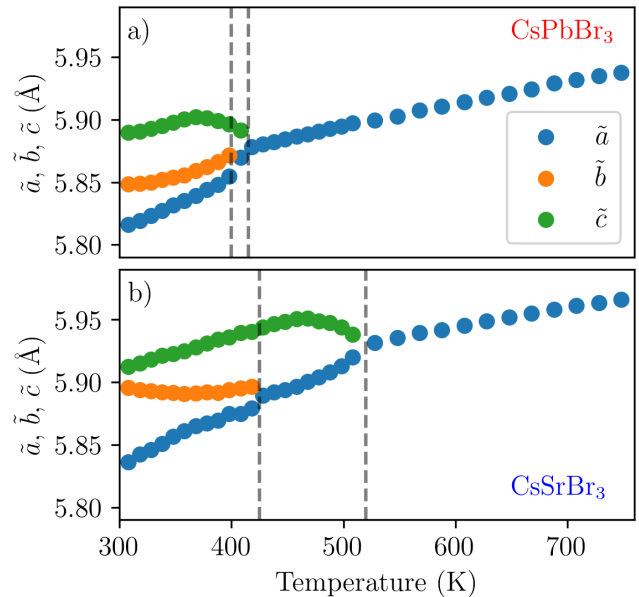


FIG. 2. **Structural properties.** Temperature-dependent lattice parameters of CsPbBr<sub>3</sub> (panel a) and CsSrBr<sub>3</sub> (panel b) determined by XRD throughout the orthorhombic—tetragonal—cubic phases. We show reduced lattice parameters  $\tilde{a}$ ,  $\tilde{b}$  and  $\tilde{c}$  for better visualization. Dashed vertical lines indicate phase-transition temperatures. Error bars from Pawley fitting are smaller than the markers and are omitted.

electronic structure, and prompts a deeper investigation of the impact of the LPE on structural dynamics.

### Lower-temperature lattice dynamics

We conduct IR and Raman spectroscopy at different temperatures as well as DFT-based harmonic-phonon calculations. The measured IR spectra show that the dominant CsSrBr<sub>3</sub> features are blue-shifted compared to those of CsPbBr<sub>3</sub> (see Figure 3a). Indeed, our DFT calculations of IR activities find a significant softening of the infrared-active TO modes in CsPbBr<sub>3</sub> compared to those in CsSrBr<sub>3</sub> (see Figure 3b): the most prominent IR-active TO mode in CsPbBr<sub>3</sub> and CsSrBr<sub>3</sub> appears at  $\sim 68$  and  $146 \text{ cm}^{-1}$ , respectively, corresponding to the same irreducible representation ( $B3u$ ) with similar eigenvectors (see Supplementary Information) in each system. This is in line with the presence of the LPE in CsPbBr<sub>3</sub> leading to a softening of particularly those phonon modes associated with the changes in dielectric properties that we reported above (*cf.* Table I), which is more relevant for the observed shifts than the difference in the atomic masses (see Supplementary Information). Moreover, the LO/TO splitting is enhanced in CsPbBr<sub>3</sub> compared to CsSrBr<sub>3</sub> and the LO phonon modes are hardened. Related to this, the CsPbBr<sub>3</sub> IR spectrum exhibits a broad feature which is known as the Reststrahlen band as has been reported before for

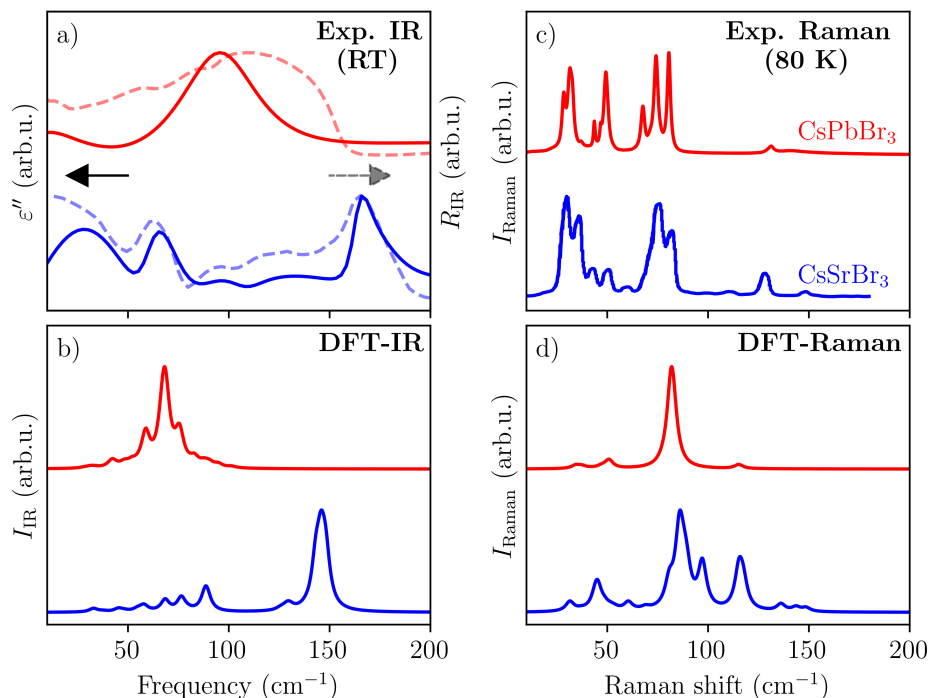


FIG. 3. **Lattice dynamics at lower temperatures.** a) IR-reflectivity spectra (dashed curves) and fitted imaginary part of the dielectric function (solid curves, see Supplemental Information for details) of CsPbBr<sub>3</sub> and CsSrBr<sub>3</sub> measured at room temperature. b) DFT-calculated IR-absorption spectra within the harmonic approximation for the orthorhombic phases. c) Raman spectra of orthorhombic CsPbBr<sub>3</sub> and CsSrBr<sub>3</sub> measured at 80 K. d) DFT-calculated Raman spectra of both compounds within the harmonic approximation for the orthorhombic phases.

MA-based HaPs.<sup>51</sup> This particular effect results in near-zero transmission through the material in a frequency range between the TO and LO modes, represented by high IR intensity values, and occurs in polar materials with larger Born-effective charges. Because the TO modes are softened and the LO modes hardened in CsPbBr<sub>3</sub> compared to CsSrBr<sub>3</sub>, and because the latter is less polar (*cf.* Table I), the absence of the LPE leads to a much less pronounced, blue-shifted Reststrahlen band appearing in a smaller frequency window in CsSrBr<sub>3</sub> (see Figure 3a, and Supplementary Information).

Figure 3c shows the 80 K Raman spectra of CsPbBr<sub>3</sub> and CsSrBr<sub>3</sub>, which are in good agreement with the Raman activities calculated for harmonic phonons (Figure 3d). Unlike IR, the Raman spectrum of CsSrBr<sub>3</sub> exhibits no substantial energy shifts with respect to CsPbBr<sub>3</sub>. Computing the phonon DOS for the orthorhombic phase of both compounds with DFT (see Supplementary Information), we find that they exhibit similar phonon DOS below 100 cm<sup>-1</sup>, *i.e.*, in the region of most of the Raman-active modes. The similar phonon DOS and the contributions of the M-site at low frequencies explain the limited shift of the CsSrBr<sub>3</sub> Raman spectrum. Above this range, CsPbBr<sub>3</sub> exhibits few vibrational states while CsSrBr<sub>3</sub> shows its most pronounced phonon DOS peaks, which correspond well with the strongest IR mode calculated from the harmonic approximation.

### High-temperature lattice dynamics

A key signature of vibrational anharmonicity in HaPs at higher temperatures is the Raman central peak.<sup>26,30–32,37–39</sup> We use this feature that is nominally symmetry-forbidden in the cubic phase as a fingerprint to directly investigate how the presence of the LPE determines anharmonicity in these materials, using Raman spectroscopy and DFT-based MD simulations. Interestingly, a central peak also appears in the high-temperature Raman spectrum of the LPE-absent CsSrBr<sub>3</sub> (see Figure 4 and Supplementary Information for full temperature range). The presence of this feature in CsSrBr<sub>3</sub> shows that LPE-induced distortions are not required for the low-frequency diffusive Raman scattering and anharmonicity to occur. This result, together with the identical phase-transition sequences of both materials (see Figure 2), led us to investigate the role of tilting instabilities in CsSrBr<sub>3</sub> and CsPbBr<sub>3</sub>.

We first calculate harmonic phonon dispersions of both compounds (see Figure 5) and find these to be remarkably similar for cubic CsSrBr<sub>3</sub> and CsPbBr<sub>3</sub> in the low frequency region, in line with the aforementioned similarities in the phonon DOS of the orthorhombic phase. Specifically, both compounds exhibit the same dynamic tilting instabilities at the edge of the Brillouin zone (BZ),

governed by in-phase (M point) and three degenerate out-of-phase (R point) rotations. These rotation modes are not only active in the phase transitions, but they also have been discussed to drive the dynamic disorder of halide perovskites.<sup>4,14,52–55</sup>

We perform MD calculations of CsPbBr<sub>3</sub> and CsSrBr<sub>3</sub> in the cubic phase to calculate the frequency-resolved dynamic changes of octahedral rotation angles,  $\Phi_\alpha(\omega)$  (see Figure 6 and Equation 1 in the Methods Section). Figure 6b shows  $\Phi_\alpha(\omega)$  for CsPbBr<sub>3</sub> and CsSrBr<sub>3</sub> and indicates strong low-frequency tilting components in both CsPbBr<sub>3</sub> and CsSrBr<sub>3</sub>. Recently, a phenomenological model for the description of the temperature-dependent Raman spectra of cubic HaPs proposed the inclusion of a low-frequency anharmonic feature, which was associated with transitions between minima of a double-well potential energy surfaces<sup>39</sup> that correspond to different octahedral tiltings.<sup>54,56–58</sup> Our results confirm that substantial octahedral dynamics correspond to low-frequency features dynamically breaking the cubic symmetry in CsPbBr<sub>3</sub> and CsSrBr<sub>3</sub>.<sup>4,14,38,59,60</sup> Interestingly, this low-frequency component appears irrespective of the presence of the LPE and induces the formation of relatively long-lived (tens of ps) structural distortions (see Supplementary Information), which strongly deviate from the average cubic symmetry. This suggests that the dynamic deviations from the long-range, crystallographic structure enable the low-frequency Raman response without violating the selection rules.

We investigate the impact of the LPE on octahedral tilting tendencies<sup>30</sup> by computing the Fourier-transform of cross-correlations between rotation angles and M-site displacements,  $C_{\alpha\beta}(\omega)$  (see Equation 2 in the Methods

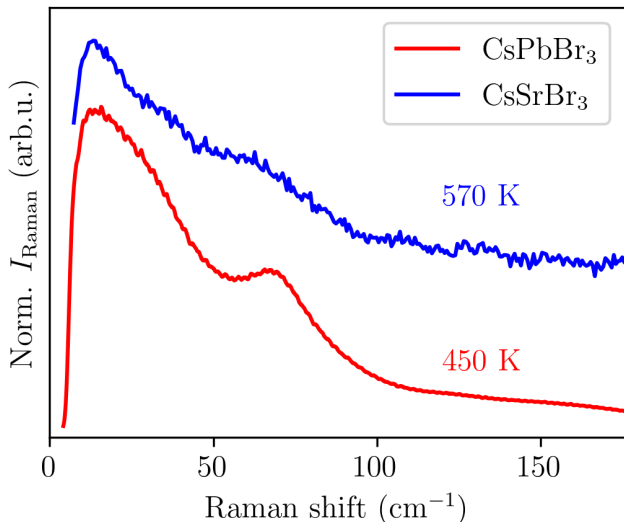


FIG. 4. **Lattice dynamics at higher temperature.** Raman spectra of CsPbBr<sub>3</sub> and CsSrBr<sub>3</sub> in the high-temperature cubic phase. The central peak appears for both compounds irrespective of the presence of LPEs.

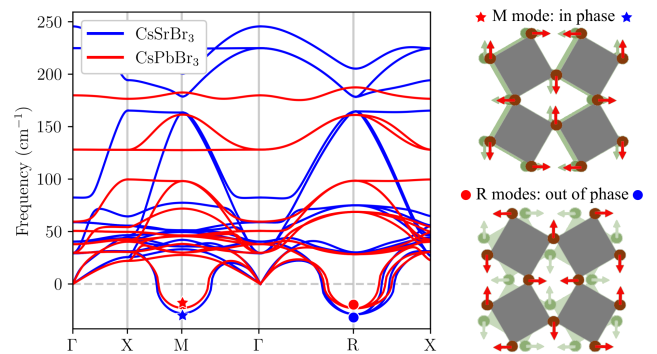


FIG. 5. **Dynamic instabilities in the lattice dynamics.** Harmonic phonon dispersion of cubic CsPbBr<sub>3</sub> and CsSrBr<sub>3</sub> showing the dynamic instabilities in the high-temperature, cubic phase of both compounds. The imaginary modes at the M and R points are the in-phase and out-of-phase tilting depicted on the right panels. The tilting modes are almost identical for CsSrBr<sub>3</sub> and CsPbBr<sub>3</sub>.

section). Larger values of  $C_{\alpha\beta}$  generally indicate stronger coupling between octahedral rotations and Pb displacements. Absence of the LPE becomes evident in the low intensity of  $C_{\alpha\beta}(\omega)$  for CsSrBr<sub>3</sub> (Figure 6c), which is less than half of that of CsPbBr<sub>3</sub>, especially at low-frequencies relevant for the slow, anharmonic, symmetry-breaking rotational features. This suggests that the presence of the LPE in CsPbBr<sub>3</sub> enhances the low-frequency octahedral tilting, in line with the literature.<sup>30</sup> However, the non-zero  $C_{\alpha\beta}$  for CsSrBr<sub>3</sub> shows that the presence of a LPE is not necessary to couple octahedral rotations and M-site displacements. We speculate that the LPE-enhanced tilting could contribute to the fact that CsPbBr<sub>3</sub> has a lower tetragonal-to-cubic phase transition temperature compared to the LPE-absent CsSrBr<sub>3</sub>.

## Discussion

HaPs are promising solar materials showing unconventional combinations of favorable optoelectronic properties and anharmonicity in their soft structures. In the search for explanations of this confluence, the presence and stereochemical activity of the LPE have been proposed as possible chemical influences. However, when controlling these effects *via* composition of HaPs one also changes ionic sizes and with it the energy scale of octahedral tilting, which inherently modulates the extent of anharmonicity. This complication had to date hindered a precise separation of structural and chemical effects in the lattice dynamic of these materials.

Here, we directly disentangled these effects by comparing CsPbBr<sub>3</sub> and CsSrBr<sub>3</sub>, two HaP compounds with similar ionic radii and structural properties but entirely different orbital interactions that leave CsSrBr<sub>3</sub> without the ability to form a LPE. Growth of CsSrBr<sub>3</sub> and CsPbBr<sub>3</sub> single crystals, and the combination of XRD, IR and Raman spectroscopy with first-principles calculations, enabled

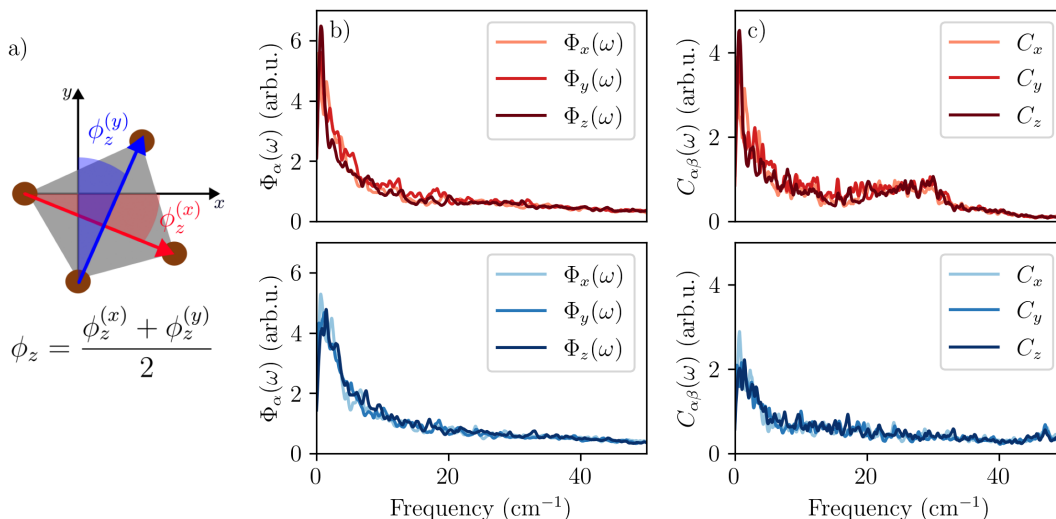


FIG. 6. **Impact of LPE on octahedral dynamics at higher temperature.** a) Schematic representation of the  $\text{MBr}_6$  octahedron aligned along the  $z$  Cartesian axis. The octahedral rotation angle around  $z$ ,  $\phi_z$ , is defined as the average of the angles formed by the  $x/y$  Cartesian axis and the vector connecting two in-plane Br atoms at opposing edges of the octahedron ( $\phi_z^{(x)}$  in red and  $\phi_z^{(y)}$  in blue). Note that a clockwise rotation is defined as positive and counter-clockwise as negative. b) Fourier transform of the octahedral rotation angle,  $\Phi_\alpha(\omega)$ , and c) cross-correlation between rotation angle and M-site displacement,  $C_{\alpha\beta}(\omega)$ , calculated using DFT-MD trajectories of cubic  $\text{CsPbBr}_3$  (upper panels, 525 K) and  $\text{CsSrBr}_3$  (lower panels, 570 K).

us to precisely investigate the role of the LPE in the anharmonic effects. We found that the electronic structure associated with the formation of a LPE is paramount for the optoelectronic properties of HaPs, because its absence resulted in large changes in dielectric screening, the direct nature of the band gap, and the carrier effective masses.<sup>26</sup> However, using the Raman central peak at higher temperatures as a fingerprint to detect anharmonicity, we found it to appear also for the LPE-absent  $\text{CsSrBr}_3$ . Our MD calculations showed that the presence of the Raman central peak correlates with the occurrence of prominent low-frequency features of slow, anharmonic rotations of the octahedra. Altogether, these findings demonstrate that the perovskite structure allows for anharmonic vibrational dynamics to occur, irrespective of the presence of the LPE, which establishes this somewhat unusual behavior as a generic effect in this material class. Since these octahedral dynamics impact the optoelectronic characteristics of these systems, our results have implications for synthesis of new HaPs with improved properties for technological applications. For instance, Pb-Sr alloying has been proposed as a method to tune the band gap of HaPs for light emission and absorption applications.<sup>41</sup> Our work implies that such Sr alloying for tuning electronic and dielectric properties preserves the strongly anharmonic lattice dynamics.

The relevance of these findings for material design strategies of HaP compounds is seen when putting our results in the context of previous work discussing anharmonic effects in this class of materials. Specifically, cubic  $\text{CsPbBr}_3$ ,  $\text{CsSnBr}_3$ ,  $\text{CsGeBr}_3$ ,  $(\text{CH}_3\text{NH}_3)_{0.13}(\text{CH}_3\text{CH}_2\text{NH}_3)_{0.87}\text{PbBr}_3$ ,

$\text{CH}(\text{NH}_2)_2\text{PbBr}_3$ , and, here,  $\text{CsSrBr}_3$  are all reported to exhibit dynamic hopping between low symmetry minima on the potential energy surface.<sup>30–32,61</sup> By contrast, the high symmetry phase of  $\text{Cs}_2\text{AgBiBr}_6$  is anharmonically stabilized and exhibits well-defined normal modes and a soft-mode transition on cooling.<sup>36</sup>  $\text{Cs}_2\text{SnBr}_6$ , on the other hand, lacks any phase transitions and similarly exhibits well-defined normal modes.<sup>62</sup> Where previously the strength of the LPE distortion or the density of cations with LPE appeared to be a plausible predictor of broad, nominally symmetry-forbidden Raman scattering resulting in a central peak, our work suggests that instead the differing symmetry in both the structure and the chemical bonding of metal halide perovskites and double-perovskites may be a controlling factor.

In conclusion, the  $ns^2$  electron configuration in HaPs that can result in a LPE is crucial to several favorable electronic features<sup>26,33,40</sup> and gives rise to the elevated ionic dielectric response *via* enhancement of Born effective charges.<sup>33,42</sup> However, we found that presence of a LPE is not necessary to produce dynamic symmetry-breaking of the sort that gives rise to broad, intense Raman scattering in the high temperature phases of HaPs and that has been associated with the unique optoelectronic properties in these compounds such as long charge-carrier lifetimes and photoinstabilities. Instead, such dynamic symmetry breaking is common to all cubic bromide and iodide (single-)perovskites thus far studied to the best of our knowledge. These results highlight the key role of structural chemistry in the anharmonic dynamics of halide perovskites, providing a new criterion for the design of soft optoelectronic semiconductors.

## METHODS

### Electronic Structure Calculations

DFT calculations were performed with Vienna ab-initio simulation package (VASP) code<sup>63</sup> using the projector-augmented wave (PAW) method.<sup>64</sup> We employed the Perdew-Burke-Ernzerhof (PBE) exchange-correlation functional<sup>65</sup> and the Tkatchenko-Scheffler (TS) scheme<sup>66</sup> – using an iterative Hirshfeld partitioning of the charge density<sup>67,68</sup> – to account for dispersive interactions. This setup has been shown to accurately describe the structure of HaPs.<sup>69,70</sup> All static calculations used an energy convergence threshold of  $10^{-6}$  eV, a plane-wave cutoff of 500 eV, and a  $\Gamma$ -centered  $k$ -grid of  $6 \times 6 \times 6$  ( $6 \times 4 \times 6$ ) for the  $Pm\bar{3}m$  ( $Pnma$ ) structures. Lattice parameters were optimized by a fitting procedure using the Birch-Murnaghan equation of state<sup>71,72</sup>. The final structures used in all subsequent calculations were obtained by relaxing the ionic degrees of freedom until the maximum residual force was below  $10^{-4}$  eV/Å. The total and projected electronic DOS and COHP, were calculated by partitioning the DFT-calculated band structure into bonding and antibonding contributions using the LOBSTER code.<sup>73,74</sup> For this task, the DFT-computed electronic wave functions were projected onto Slater-type orbitals (basis set name: "pbeVaspFit2015")<sup>73</sup> including Cs 6s, 5p and 5s, Pb 6s and 6p, and Br 4p and 4s states. The maximum charge spilling in this procedure was 1.3%. Spin-orbit coupling was not included in our calculations, since it is currently not supported by the LOBSTER code. We emphasize that our focus is on the orbital contributions to the (anti) bonding interactions, rather than on a quantitative descriptions of the energy.

### Phonon Calculations

Phonon dispersions and DOSs were obtained *via* the finite displacements method implemented in the phonopy package.<sup>75</sup> For these calculations, we used  $2 \times 2 \times 2$  supercells with 40 (160) atoms of the  $Pm\bar{3}m$  ( $Pnma$ ) CsMBr<sub>3</sub> structures reducing  $k$ -space sampling accordingly. IR and Raman spectra were computed with the phonopy-spectroscopy package,<sup>76</sup> using zone-center phonon modes, Born-effective charges and polarizabilities, calculated with density functional perturbation theory (DFPT).<sup>77</sup>

### First-principles Molecular Dynamics

DFT-based MD calculations were performed for  $2 \times 2 \times 2$  supercells of the  $Pm\bar{3}m$  structures using a Nosé-Hoover thermostat within the canonical ensemble (NVT), as implemented in VASP.<sup>78</sup> The simulation temperature was set to  $T=525$  and 570 K for CsPbBr<sub>3</sub> and CsSrBr<sub>3</sub>, respectively. An 8 fs timestep, reduced  $k$ -grid of  $3 \times 3 \times 3$ , and energy convergence threshold of  $10^{-5}$  eV were used for the 10 ps equilibration and 115 ps production runs.

### Octahedral Rotation Dynamics and Cross-correlations

We quantified the octahedral dynamics using the rotation angles,  $\phi_\alpha$ , around a given Cartesian axis  $\alpha$  (see Figure 6a). The frequency-resolved rotational dynamics were calculated as the Fourier transform of  $\phi_\alpha$ :

$$\Phi_\alpha(\omega) = \frac{1}{N_{\text{steps}}} \int_0^\infty \phi_\alpha(t) e^{-i\omega t} dt, \quad (1)$$

where  $N_{\text{steps}}$  is the number of snapshots. To compute the angles we selected 1000 equally spaced snapshots. We calculated the frequency-resolved cross-correlation between octahedral rotation angles (around a Cartesian direction  $\alpha$ ) and the displacements (along a Cartesian direction  $\beta$ ) of the corresponding M-site,  $d_\beta^M(t)$ , as:

$$C_{\alpha\beta}(\omega) = \frac{1}{N_{\text{steps}}} \int_0^\infty \frac{\langle \phi_\alpha(t + \delta t) \cdot d_\beta^M(t) \rangle}{\langle \phi_\alpha(t) \cdot d_\beta^M(t) \rangle} e^{-i\omega t} dt. \quad (2)$$

### Polycrystalline Sample Preparation

CsBr (Alfa Aesar, 99.9%), anhydrous SrBr<sub>2</sub> (Alfa Aesar, 99%), Cs<sub>2</sub>CO<sub>3</sub>, PbO, and concentrated aqueous HBr were purchased and used as received. Guided by the reported pseudo-binary phase diagram,<sup>79</sup> polycrystalline CsSrBr<sub>3</sub> for X-ray powder diffraction and Raman spectroscopy was prepared by a solid-state reaction at 600 °C. CsBr (5 mmol, 1064 mg) and SrBr<sub>2</sub> (5 mmol, 1237 mg) were ground and pressed into a 5 mm diameter pellet, placed in an alumina crucible, and flame-sealed under  $\sim 1/3$  atmosphere of argon in a fused silica ampoule. The reaction yields a porous, colorless pellet which is easily separated from the crucible and ground in inert atmosphere. Polycrystalline CsPbBr<sub>3</sub> for X-ray powder diffraction was prepared in ambient atmosphere by precipitation from aqueous hydrobromic acid. PbO (2 mmol, 446.4 mg) was dissolved in 2 mL hot concentrated HBr under stirring. Cs<sub>2</sub>CO<sub>3</sub> (1 mmol, 325.8 mg) was added slowly resulting in an immediate bright orange precipitate. 13 mL additional HBr was added and the mixture left to stir. After an hour, stirring was stopped and the mixture allowed to cool to room temperature. Excess solution was decanted, and the remaining mixture was evaporated to dryness on a hotplate and ground. Phase purity of all prepared compounds was established by powder XRD.

### Single Crystal Preparation

Single crystals of CsSrBr<sub>3</sub> were grown by the Bridgman method from a stoichiometric mixture of the binary metal bromides in a 10 mm diameter quartz ampoule. CsSrBr<sub>3</sub> was pulled at 0.5 mm/h through an 800 °C hot zone, yielding a multi-crystalline rod from which several-mm single crystal regions could be cleaved.

CsSrBr<sub>3</sub> is extremely hygroscopic and all preparation and handling was performed in an inert atmosphere.

The vertical Bridgman method was used to grow large, high-quality single crystals of CsPbBr<sub>3</sub>. After synthesis and purification (see Supplemental Information for details), the ampoule was reset to the hot zone for the Bridgman Growth. The zone 1 temperature was set to 650 °C with a 150 °C/h ramp rate, and held for 12 h to ensure a full melt before sample motion occurred. The zone 2 and 3 temperatures were set to 375 °C. These temperatures were held for 350 h while the ampoule was moved through the furnace at a rate of 0.9 mm/h under 0.3 rpm rotation. After the motion had ceased, the zone 1 temperature ramped to 375 °C to make the temperature profile in the furnace uniform. The cooling program was set to slow during the phase transitions occurring near 120 and 90 °C, with a 10 °C/h cooling rate from 375 °C to 175 °C, a 2.5 °C/h slow cooling rate from 175 °C to 75 °C, and a 10 °C/h rate to 30 °C. The resulting CsPbBr<sub>3</sub> ingot was orange-red and had large ( $\geq 5$  mm) transparent single-crystalline domains, though the edges of some portions exhibited twinning.

### X-ray Diffraction

Polycrystalline samples were ground with silicon powder (as an internal standard and diluent) and packed in borosilicate glass capillaries. Powder XRD patterns were measured in Debye–Scherrer geometry using a STOE Stadi P diffractometer (Mo K <sub>$\alpha$ 1</sub> radiation, Ge-(111) monochromator, Mythen 1K Detector) equipped with a furnace. Data were analyzed by sequential Pawley refinement using GSAS-II.<sup>80</sup>

### Infrared Reflectivity Measurements

IR-reflection spectra in the THz range were measured as a combination of time-domain THz spectroscopy (TDS) for the low-frequency end and bolometer detection for the higher frequencies. Bolometer spectra were measured using a Bruker 80v Fourier-transform IR spectrometer with a globar source and a bolometer detector cooled to liquid He temperatures. The crystals were mounted for reflection measurements and the instrument was sealed in vacuum. A gold mirror was used as reflection reference. TDS was performed using a Spectra Physics Mai Tai-Empower-Spitfire Pro Ti:Sapphire regenerative

amplifier. The amplifier generates 35 fs pulses centered at 800 nm at a repetition rate of 5 kHz. THz pulses were generated by a spintronic emitter, which was composed of 1.8 nm of Co<sub>40</sub>Fe<sub>40</sub>B<sub>20</sub> sandwiched between 2 nm of Tungsten and 2 nm of Platinum, all supported by a quartz substrate. The THz pulses were detected using electro-optic sampling in a (100)-ZnTe crystal. A gold mirror was used as reflection reference. The sample crystals, THz emitter and THz detector were held under vacuum during the measurements.

TDS offers better signal at low frequency, while bolometer measurements have an advantage over TDS at higher frequencies. Therefore, the spectra were combined and merged at 100 cm<sup>-1</sup>. Owing to scattering losses, the absolute intensity of reflected light can not be taken quantitatively. Therefore, the spectra were scaled to the signal level at 100 cm<sup>-1</sup> before merging the data. The final reflectivity spectra are given in arbitrary units. The phonon frequencies and overall spectral shape allows for fitting to the dielectric function.

### Raman Spectroscopy

All the measurements were taken in a home-built back scattering Raman system. For all measurements, the laser was focused with a 50x objective (Zeiss, USA), and the Rayleigh scattering was then filtered with a notch filter (Ondax Inc., USA). The beam was focused into a spectrometer 1 m long (FHR 1000, Horiba) and then on a CCD detector. To get the unpolarized Raman spectrum for the single crystals (CsSrBr<sub>3</sub> low temperatures and CsPbBr<sub>3</sub>), two orthogonal angles were measured in parallel and cross configurations (four measurements overall). The unpolarized spectrum is a summation of all four spectra. The samples were cooled below room temperature by a Janis cryostat ST-500 controlled by Lakeshore model 335 and were heated above room temperature by a closed heating system (Linkam Scientific). Due to the extreme sensitivity of CsSrBr<sub>3</sub> to ambient moisture, CsSrBr<sub>3</sub> powder was flame-sealed in a small quartz capillary for the high-temperature measurements, and a single crystal was loaded into a closed cell under an Ar environment for the low temperatures measurements. CsSrBr<sub>3</sub> low temperature measurements were taken with a 2.5 eV CW diode laser (Coherent Inc.). CsSrBr<sub>3</sub> high-temperature measurement and all the CsPbBr<sub>3</sub> measurements were taken with a 1.57 eV CW diode laser (Coherent Inc.).

\* Present address: Department of Materials Science and Engineering, University of Texas at Dallas, 75080 Richardson, TX, USA

† dhfabini@gmail.com

‡ david.egger@tum.de

<sup>1</sup> Snaith, H. J. Perovskites: The emergence of a new era for low-cost, high-efficiency solar cells. *J. Phys. Chem. Lett.* **4**,

3623–3630 (2013).

<sup>2</sup> Correa-Baena, J.-P. *et al.* Promises and challenges of perovskite solar cells. *Science* **358**, 739–744 (2017).

<sup>3</sup> Nayak, P. K., Mahesh, S., Snaith, H. J. & Cahen, D. Photovoltaic solar cell technologies: analysing the state of the art. *Nat. Rev. Mater.* **4**, 269–285 (2019).

<sup>4</sup> Beecher, A. N. *et al.* Direct Observation of Dynamic Sym-

- metry Breaking above Room Temperature in Methylammonium Lead Iodide Perovskite. *ACS Energy Lett.* **1**, 880–887 (2016). 1606.09267.
- 5 Whalley, L. D., Skelton, J. M., Frost, J. M. & Walsh, A. Phonon anharmonicity, lifetimes, and thermal transport in  $\text{CH}_3\text{NH}_3\text{PbI}_3$  from many-body perturbation theory. *Phys. Rev. B* **94**, 1–5 (2016).
  - 6 Carignano, M. A., Aravindh, S. A., Roqan, I. S., Even, J. & Katan, C. Critical Fluctuations and Anharmonicity in Lead Iodide Perovskites from Molecular Dynamics Supercell Simulations. *J. Mater. Chem. C* **121**, 20729–20738 (2017).
  - 7 Brenner, T. M., Egger, D. A., Kronik, L., Hodes, G. & Cahen, D. Hybrid organic–inorganic perovskites: low-cost semiconductors with intriguing charge-transport properties. *Nat. Rev. Mater.* **1**, 15007 (2016). 1011.1669v3.
  - 8 Egger, D. A. *et al.* What remains unexplained about the properties of halide perovskites? *Adv. Mater.* **30**, 1800691 (2018).
  - 9 Ceratti, D. R. *et al.* Self-Healing Inside  $\text{APbBr}_3$  Halide Perovskite Crystals. *Adv. Mater.* **30**, 1706273 (2018).
  - 10 Cahen, D., Kronik, L. & Hodes, G. Are Defects in Lead-Halide Perovskites Healed, Tolerated, or Both? *ACS Energy Lett.* 4108–4114 (2021).
  - 11 Parida, S. *et al.* Self-Healing and -Repair of Nanomechanical Damages in Lead Halide Perovskites. *Adv Funct Materials* 2304278 (2023).
  - 12 Patrick, C. E., Jacobsen, K. W. & Thygesen, K. S. Anharmonic stabilization and band gap renormalization in the perovskite  $\text{CsSnI}_3$ . *Phys. Rev. B* **92**, 201205 (2015).
  - 13 Wiktor, J., Rothlisberger, U. & Pasquarello, A. Predictive Determination of Band Gaps of Inorganic Halide Perovskites. *J. Phys. Chem. Lett.* **8**, 5507–5512 (2017).
  - 14 Lanigan-Atkins, T. *et al.* Two-dimensional overdamped fluctuations of the soft perovskite lattice in  $\text{CsPbBr}_3$ . *Nat. Mater.* **20**, 977–983 (2021).
  - 15 Seidl, S. A. *et al.* Anharmonic fluctuations govern the band gap of halide perovskites. *Phys. Rev. Materials* **7**, L092401 (2023).
  - 16 Gehrman, C. & Egger, D. A. Dynamic shortening of disorder potentials in anharmonic halide perovskites. *Nat. Commun.* **10**, 3141 (2019).
  - 17 Gehrman, C., Caicedo-Dávila, S., Zhu, X. & Egger, D. A. Transversal Halide Motion Intensifies Band-To-Band Transitions in Halide Perovskites. *Adv. Sci.* **9**, 2200706 (2022).
  - 18 Wu, B. *et al.* Indirect tail states formation by thermal-induced polar fluctuations in halide perovskites. *Nat. Commun.* **10**, 1–10 (2019).
  - 19 Mayers, M. Z., Tan, L. Z., Egger, D. A., Rappe, A. M. & Reichman, D. R. How Lattice and Charge Fluctuations Control Carrier Dynamics in Halide Perovskites. *Nano Lett.* **18**, 8041–8046 (2018).
  - 20 Lacroix, A., De Laissardière, G. T., Quémerais, P., Julien, J. P. & Mayou, D. Modeling of Electronic Mobilities in Halide Perovskites: Adiabatic Quantum Localization Scenario. *Phys. Rev. Lett.* **124**, 1–6 (2020).
  - 21 Iaru, C. M. *et al.* Fröhlich interaction dominated by a single phonon mode in  $\text{CsPbBr}_3$ . *Nat. Commun.* **12**, 5844 (2021).
  - 22 Schilcher, M. J. *et al.* The Significance of Polarons and Dynamic Disorder in Halide Perovskites. *ACS Energy Lett.* **6**, 2162–2173 (2021).
  - 23 Lai, R. *et al.* Transient Suppression of Carrier Mobility Due to Hot Optical Phonons in Lead Bromide Perovskites. *J. Phys. Chem. Lett.* **13**, 5488–5494 (2022).
  - 24 Zhang, K.-C., Shen, C., Zhang, H.-B., Li, Y.-F. & Liu, Y. Effect of quartic anharmonicity on the carrier transport of cubic halide perovskites  $\text{CsSnI}_3$  and  $\text{CsPbI}_3$ . *Phys. Rev. B* **106**, 235202 (2022).
  - 25 Schilcher, M. J. *et al.* Correlated anharmonicity and dynamic disorder control carrier transport in halide perovskites. *Phys. Rev. Materials* **7**, L081601 (2023).
  - 26 Fabini, D. H., Seshadri, R. & Kanatzidis, M. G. The underappreciated lone pair in halide perovskites underpins their unusual properties. *MRS Bull.* **45**, 467–477 (2020).
  - 27 Smith, E. H., Benedek, N. A. & Fennie, C. J. Interplay of Octahedral Rotations and Lone Pair Ferroelectricity in  $\text{CsPbF}_3$ . *Inorg. Chem.* **54**, 8536–8543 (2015).
  - 28 Fabini, D. H. *et al.* Dynamic Stereochemical Activity of the  $\text{Sn}^{2+}$  Lone Pair in Perovskite  $\text{CsSnBr}_3$ . *J. Am. Chem. Soc.* **138**, 11820–11832 (2016).
  - 29 Radha, S. K., Bhandari, C. & Lambrecht, W. R. Distortion modes in halide perovskites: To twist or to stretch, a matter of tolerance and lone pairs. *Phys. Rev. Materials* **2**, 1–11 (2018).
  - 30 Gao, L. *et al.* Metal cation s lone-pairs increase octahedral tilting instabilities in halide perovskites. *Mater. Adv.* **2**, 4610–4616 (2021).
  - 31 Yaffe, O. *et al.* Local Polar Fluctuations in Lead Halide Perovskite Crystals. *Phys. Rev. Lett.* **118**, 1–6 (2017).
  - 32 Huang, X. *et al.* Understanding Electron–Phonon Interactions in 3D Lead Halide Perovskites from the Stereochemical Expression of  $6s^2$  Lone Pairs. *J. Am. Chem. Soc.* **144**, 12247–12260 (2022).
  - 33 Du, M. H. Efficient carrier transport in halide perovskites: theoretical perspectives. *J. Mater. Chem. A* **2**, 9091–9098 (2014).
  - 34 Herz, L. M. How Lattice Dynamics Moderate the Electronic Properties of Metal-Halide Perovskites. *J. Phys. Chem. Lett.* **9**, 6853–6863 (2018).
  - 35 Goldschmidt, V. M. Die Gesetze der Krystallochemie. *Naturwissenschaften* **14**, 477–485 (1926).
  - 36 Cohen, A. *et al.* Diverging expressions of anharmonicity in halide perovskites. *Adv. Mater.* **34**, 2107932 (2022).
  - 37 Ferreira, A. C. *et al.* Direct evidence of weakly dispersed and strongly anharmonic optical phonons in hybrid perovskites. *Commun. Phys.* **3**, 48 (2020).
  - 38 Sharma, R. *et al.* Elucidating the atomistic origin of anharmonicity in tetragonal  $\text{CH}_3\text{NH}_3\text{PbI}_3$  with Raman scattering. *Phys. Rev. Materials* **4**, 092401 (2020).
  - 39 Menahem, M. *et al.* Disorder origin of Raman scattering in perovskite single crystals. *Phys. Rev. Materials* **7**, 044602 (2023).
  - 40 Goesten, M. G. & Hoffmann, R. Mirrors of Bonding in Metal Halide Perovskites. *J. Am. Chem. Soc.* **140**, 12996–13010 (2018).
  - 41 Straus, D. B. & Cava, R. J. Tuning the Band Gap in the Halide Perovskite  $\text{CsPbBr}_3$  through Sr Substitution. *ACS Appl. Mater. Interfaces* (2022).
  - 42 Du, M.-H. & Singh, D. J. Enhanced Born charge and proximity to ferroelectricity in thallium halides. *Phys. Rev. B* **81**, 144114 (2010).
  - 43 Sun, J. & Singh, D. J. Electronic Properties, Screening, and Efficient Carrier Transport in  $\text{NaSbS}_2$ . *Phys. Rev. Applied* **7**, 024015 (2017).
  - 44 Ran, Z. *et al.* Bismuth and antimony-based oxyhalides and chalcogenides as potential optoelectronic materials. *npj Comput Mater* **4**, 14 (2018).
  - 45 Kang, B. & Biswas, K. Exploring Polaronic, Excitonic Structures and Luminescence in  $\text{Cs}_4\text{PbBr}_6/\text{CsPbBr}_3$ . *J.*

- Phys. Chem. Lett.* **9**, 830–836 (2018).
- <sup>46</sup> Rodová, M., Brožek, J. & Nitsch, K. Phase transitions in ternary caesium lead bromide. *J. Therm. Anal.* **71**, 667–673 (2003).
- <sup>47</sup> Stoumpos, C. C. *et al.* Crystal Growth of the Perovskite Semiconductor CsPbBr<sub>3</sub>: A New Material for High-Energy Radiation Detection. *Cryst. Growth Des.* **13**, 2722–2727 (2013).
- <sup>48</sup> Loyd, M. *et al.* Crystal structure and thermal expansion of CsCaI<sub>3</sub>:Eu and CsSrBr<sub>3</sub>:Eu scintillators. *J. Cryst. Growth* **481**, 35–39 (2018).
- <sup>49</sup> Fabini, D. H. *et al.* Reentrant Structural and Optical Properties and Large Positive Thermal Expansion in Perovskite Formamidinium Lead Iodide. *Angew. Chem. Int. Ed.* **55**, 15392–15396 (2016).
- <sup>50</sup> Schueller, E. C. *et al.* Crystal Structure Evolution and Notable Thermal Expansion in Hybrid Perovskites Formamidinium Tin Iodide and Formamidinium Lead Bromide. *Inorg. Chem.* **57**, 695–701 (2018).
- <sup>51</sup> Sendner, M. *et al.* Optical phonons in methylammonium lead halide perovskites and implications for charge transport. *Mater. Horiz.* **3**, 613–620 (2016).
- <sup>52</sup> Armstrong, R. L. Displacive order—disorder crossover in perovskite and antiferroelectric crystals undergoing rotational phase transitions. *Prog. Nucl. Magn. Reson. Spectrosc.* **21**, 151–173 (1989).
- <sup>53</sup> Woodward, P. M. Octahedral Tilting in Perovskites. I. Geometrical Considerations. *Acta Crystallogr B* **53**, 32–43 (1997).
- <sup>54</sup> Yang, R. X., Skelton, J. M., Da Silva, E. L., Frost, J. M. & Walsh, A. Spontaneous octahedral tilting in the cubic inorganic cesium halide perovskites CsSnX<sub>3</sub> and CsPbX<sub>3</sub> (X = F, Cl, Br, I). *J. Phys. Chem. Lett.* **8**, 4720–4726 (2017).
- <sup>55</sup> Yang, R. X., Skelton, J. M., da Silva, E. L., Frost, J. M. & Walsh, A. Assessment of dynamic structural instabilities across 24 cubic inorganic halide perovskites. *J. Chem. Phys.* **152**, 024703 (2020).
- <sup>56</sup> Klarbring, J. Low-energy paths for octahedral tilting in inorganic halide perovskites. *Phys. Rev. B* **99**, 1–7 (2019). 1802.09632.
- <sup>57</sup> Bechtel, J. S., Thomas, J. C. & Van Der Ven, A. Finite-temperature simulation of anharmonicity and octahedral tilting transitions in halide perovskites. *Phys. Rev. Materials* **3**, 113605 (2019).
- <sup>58</sup> Zhu, X., Caicedo-Dávila, S., Gehrman, C. & Egger, D. A. Probing the Disorder Inside the Cubic Unit Cell of Halide Perovskites from First-Principles. *ACS Appl. Mater. Interfaces* **14**, 22973–22981 (2022).
- <sup>59</sup> Wiktor, J., Fransson, E., Kubicki, D. & Erhart, P. Quantifying Dynamic Tilting in Halide Perovskites: Chemical Trends and Local Correlations (2023). URL <http://arxiv.org/abs/2304.07402>. 2304.07402.
- <sup>60</sup> Baldwin, W. J. *et al.* Dynamic Local Structure in Caesium Lead Iodide: Spatial Correlation and Transient Domains. *Small* **2303565** (2023).
- <sup>61</sup> Reuveni, G. *et al.* Static and dynamic disorder in formamidinium lead bromide single crystals. *J. Phys. Chem. Lett.* **14**, 1288–1293 (2023).
- <sup>62</sup> Kaltzoglou, A. *et al.* Optical-vibrational properties of the Cs<sub>2</sub>SnX<sub>6</sub> (X = Cl, Br, I) defect perovskites and hole-transport efficiency in dye-sensitized solar cells. *J. Phys. Chem. C* **120**, 11777–11785 (2016).
- <sup>63</sup> Kresse, G. & Furthmüller, J. Efficient iterative schemes for ab initio total-energy calculations using a plane-wave basis set. *Phys. Rev. B* **54**, 11169–11186 (1996).
- <sup>64</sup> Kresse, G. & Joubert, D. From ultrasoft pseudopotentials to the projector augmented-wave method. *Phys. Rev. B* **59**, 1758–1775 (1999).
- <sup>65</sup> Perdew, J. P., Burke, K. & Ernzerhof, M. Generalized gradient approximation made simple. *Phys. Rev. Lett.* **77**, 3865–3868 (1996).
- <sup>66</sup> Tkatchenko, A. & Scheffler, M. Accurate Molecular Van Der Waals Interactions from Ground-State Electron Density and Free-Atom Reference Data. *Phys. Rev. Lett.* **102**, 073005 (2009).
- <sup>67</sup> Bučko, T., Lebègue, S., Hafner, J. & Ángyán, J. G. Improved density dependent correction for the description of London dispersion forces. *J. Chem. Theory Comput.* **9**, 4293–4299 (2013).
- <sup>68</sup> Bučko, T., Lebègue, S., Ángyán, J. G. & Hafner, J. Extending the applicability of the Tkatchenko-Scheffler dispersion correction via iterative Hirshfeld partitioning. *J. Chem. Phys.* **141**, 034114 (2014).
- <sup>69</sup> Egger, D. A. & Kronik, L. Role of dispersive interactions in determining structural properties of organic-inorganic halide perovskites: Insights from first-principles calculations. *J. Phys. Chem. Lett.* **5**, 2728–2733 (2014).
- <sup>70</sup> Beck, H., Gehrman, C. & Egger, D. A. Structure and binding in halide perovskites: Analysis of static and dynamic effects from dispersion-corrected density functional theory. *APL Mater.* **7**, 021108 (2019).
- <sup>71</sup> Birch, F. Finite Elastic Strain of Cubic Crystals. *Phys. Rev.* **71**, 809–824 (1947).
- <sup>72</sup> Murnaghan, F. D. The Compressibility of Media under Extreme Pressures. *Proc. Natl. Acad. Sci. U.S.A.* **30**, 244–247 (1944).
- <sup>73</sup> Maintz, S., Deringer, V. L., Tchougréeff, A. L. & Drnaskowski, R. LOBSTER: A tool to extract chemical bonding from plane-wave based DFT. *J. Comput. Chem.* **37**, 1030–1035 (2016).
- <sup>74</sup> Nelson, R. *et al.* LOBSTER : Local orbital projections, atomic charges, and chemical-bonding analysis from PROJECTOR-AUGMENTED-WAVE-BASED density-functional theory. *J Comput Chem* **41**, 1931–1940 (2020).
- <sup>75</sup> Togo, A. & Tanaka, I. First principles phonon calculations in materials science. *Scripta Materialia* **108**, 1–5 (2015).
- <sup>76</sup> Skelton, J. M. *et al.* Lattice dynamics of the tin sulphides SnS<sub>2</sub>, SnS and Sn<sub>2</sub>S<sub>3</sub>: vibrational spectra and thermal transport. *Phys. Chem. Chem. Phys.* **19**, 12452–12465 (2017).
- <sup>77</sup> Gajdoš, M., Hummer, K., Kresse, G., Furthmüller, J. & Bechstedt, F. Linear optical properties in the projector-augmented wave methodology. *Phys. Rev. B* **73**, 1–9 (2006).
- <sup>78</sup> Kresse, G. & Hafner, J. Ab initio molecular-dynamics simulation of the liquid-metalamorphous- semiconductor transition in germanium. *Phys. Rev. B* **49**, 14251–14269 (1994).
- <sup>79</sup> Riccardi, R., Sinistri, C., Campari, G. Y. & Magistris, A. Binary systems formed by alkali bromides with barium or strontium bromide. *Z. Naturforsch. A* **25**, 781–785 (1970).
- <sup>80</sup> Toby, B. H. & Dreele, R. B. V. *GSAS-II*: the genesis of a modern open-source all purpose crystallography software package. *J. Appl. Crystallogr.* **46**, 544–549 (2013).

## Acknowledgements

Funding provided by the Alexander von Humboldt-

Foundation in the framework of the Sofja Kovalevskaja Award, endowed by the German Federal Ministry of Education and Research, by the Deutsche Forschungsgemeinschaft (DFG, German Research Foundation) *via* Germany's Excellence Strategy - EXC 2089/1-390776260, and by TU Munich - IAS, funded by the German Excellence Initiative and the European Union Seventh Framework Programme under Grant Agreement No. 291763, are gratefully acknowledged. Funding was provided by the Engineering and Physical Sciences Research Council (EPSRC), UK. The Gauss Centre for Supercomputing e.V. is acknowledged for providing computing time through the John von Neumann Institute for Computing on the GCS Supercomputer JUWELS at Jülich Supercomputing Centre. D.H.F. gratefully acknowledges financial support from the Alexander von Humboldt Foundation and the Max Planck Society. D.H.F. thanks Maximilian A. Plass for assistance with flame-sealing the Raman capillaries. K.M.M. and

M.V.K. acknowledge financial support by ETH Zürich through the ETH+ Project SynMatLab "Laboratory for Multiscale Materials Synthesis."

### Author contributions

S.C.-D. performed the theoretical calculations, analyzed the data and wrote the initial manuscript under the supervision of D.A.E. A.C. performed Raman measurements and analyzed data under the supervision of O.Y. S.M. performed IR measurements and analyzed data under the supervision of L.M.H. D.H.F. prepared polycrystalline samples, performed XRD measurements, and analyzed data. M.I. prepared the CsSrBr<sub>3</sub> single crystals. K.M.M. prepared the CsPbBr<sub>3</sub> single crystals under the supervision of M.V.K. D.H.F. and D.A.E. conceived and supervised the project.